

Supporting Information

Water Reactivity on the LaCoO₃ (001) Surface: An Ambient Pressure X-ray Photoelectron Spectroscopy Study

Kelsey A. Stoerzinger^{1,‡,*}, Wesley T. Hong^{1,‡}, Ethan J. Crumlin³, Hendrik Bluhm⁴, Michael D. Biegalski⁵, Yang Shao-Horn^{1,2,*}

¹ Department of Materials Science & Engineering,

² Department of Mechanical Engineering, Massachusetts Institute of Technology,
Cambridge, MA 02139, USA

³ Advanced Light Source, Lawrence Berkeley National Laboratory, Berkeley, CA 94720 USA

⁴ Chemical Sciences Division, Lawrence Berkeley National Laboratory,
Berkeley, CA 94720 USA

⁵ Center for Nanophase Materials Sciences, Oak Ridge National Laboratory,
Oak Ridge, TN 37831 USA

Index	Page
Error analysis	S1-S5
Figures and Tables	S6-S20
References	S21-22

Estimating Uncertainty in Peak Fitting Parameters

Uncertainties in the fitted peak areas, binding energies, and full-width-half-maxima were determined using a Monte Carlo method to obtain the covariance matrix of the fitted parameters, assuming a Poisson noise distribution function (CasaXPS). Next to the validity of the fitting model, the selection of the noise distribution function is generally the weakest point of the accuracy for this form of error analysis. In order to verify the validity of the Poisson assumption, a region absent of core-level excitations can be analyzed by a linear regression that minimizes:

$$\chi^2 = \sum_{i=1}^n \left(\frac{d_i - [a(E_i - P_{\text{region}}) + b]}{\sigma_i} \right)^2$$

where $\{d_1, d_2, \dots, d_n\}$ are the measured data intensities corresponding to energies $\{E_1, E_2, \dots, E_n\}$ with standard deviations $\{\sigma_1, \sigma_2, \dots, \sigma_n\}$, and a , b and P_{region} are linear parameters defined by the region. A standardized residual (normalized to the square root of the counts per second, i.e. the standard deviation of a Poisson distribution) close to unity then suggests that the noise in the data channels obeys Poisson statistics. Standardized residuals obtained after linear regression of the O 1s region absent of any peaks were found to be ~ 0.99 , which suggests that this method of error analysis reliably captures the uncertainty associated with the experimental noise and parametric fitting of the spectra.

A total of 400 samples for each experimental condition were simulated by this method. The histograms for the O 1s fitted peak areas at 300 °C and 50 °C in 0.1 Torr H₂O is shown in Fig. S10 and S11 (with equal numbers of bins for each species). Note the wider spread and non-normal distributions that can result from the correlation between peak components with low intensities (e.g., OH, CO₃, and H₂O_{ads}). The low areas for CO₃ and H₂O_{ads} species result in a distribution wider than the range of the x-axis. With the better defined peak features in the raw spectra at lower temperatures (e.g., 50 °C), the spreads are significantly reduced and the fitted peak areas approach normal-like distributions.

The sampling distribution of the fitted peak areas obtained from each simulation of the Monte Carlo analysis can then be used to calculate the mean coverage and determine their uncertainty. Error bars for the coverages were defined as the 95% confidence intervals (**Fig. 9 and 10**), determined as the 2.5% and 97.5% quantiles of the simulated sampling distribution due

to the non-normal behavior of the fitted fit areas. We note that this measure of error only captures the noise in the data and the parametric fitting of the peaks; it does not reflect the reliability of the peak fitting constraints (e.g. number of peaks) or the electron attenuation model used.

Details of surface adsorbate coverage calculations

Our model treats each species as a continuum slab in a multilayer configuration, characterized by its oxygen atomic density (N), photoionization cross section (σ), thickness (t), coverage (θ), and inelastic mean free path (λ). A schematic illustration of the slabs is shown in **Fig. 8**. It is postulated that the “Surface” oxygen layer includes perovskite CoO_2 and LaO terminations and/or reconstructed perovskite surfaces, and was treated as a slab of complete coverage but with variable thickness. The parameters used in the model for this layer were those of the LCO crystal structure, as shown in **Table S4**. OH and CO_3 were considered to co-adsorb on the film surface, with component thickness fixed at $t_{\text{OH}} = 3.0 \text{ \AA}$ based on $\text{Co}(\text{OH})_2^1$ and $t_{\text{CO}_3} = 4.5 \text{ \AA}$ based on $\text{La}_2(\text{CO}_3)_3 \cdot 8\text{H}_2\text{O}^2$ (**Table S4**). Although the combined coverage was allowed to vary, the computed values remained less than one monolayer. Finally, adsorbed water found at low temperatures and high RHs was considered to cover the entire surface with variable thickness $t_{\text{H}_2\text{O}}$. Although adsorbed water likely binds preferentially to OH and less so to CO_3 , our model describes adsorbed water covering both adsorbates, as it is assumed that any phase segregation of surface species such as OH and CO_3 is smaller than the area from which XPS data were collected.

The XPS intensities (I) of all components in the model were expressed as below, where λ is defined as the mean free path component along the surface normal, accounting for the emission angle of photoelectrons from the surface normal (42° in the current setup), i.e. $\lambda = \lambda' \cos(42^\circ)$. N was determined from the density and oxygen stoichiometry of reference compounds (**Table S4**),

and σ assumed to vary little in the < 5 eV binding energy difference from bulk oxygen to adsorbed water.

$$I_{\text{H}_2\text{O}} \sim N_{\text{H}_2\text{O}} \sigma_{\text{H}_2\text{O}} \lambda_{\text{H}_2\text{O}} \left[1 - \exp\left(-\frac{t_{\text{H}_2\text{O}}}{\lambda_{\text{H}_2\text{O}}}\right) \right] \quad (1a)$$

$$I_{\text{OH}} \sim N_{\text{OH}} \sigma_{\text{OH}} \lambda_{\text{OH}} \theta_{\text{OH}} \exp\left(-\frac{t_{\text{H}_2\text{O}}}{\lambda_{\text{H}_2\text{O}}}\right) \left[1 - \exp\left(-\frac{t_{\text{OH}}}{\lambda_{\text{OH}}}\right) \right] \quad (1b)$$

$$I_{\text{CO}_3} \sim N_{\text{CO}_3} \sigma_{\text{CO}_3} \lambda_{\text{CO}_3} \theta_{\text{CO}_3} \exp\left(-\frac{t_{\text{H}_2\text{O}}}{\lambda_{\text{H}_2\text{O}}}\right) \left[1 - \exp\left(-\frac{t_{\text{CO}_3}}{\lambda_{\text{CO}_3}}\right) \right] \quad (1c)$$

$$I_{\text{surf}} \sim N_{\text{surf}} \sigma_{\text{surf}} \lambda_{\text{surf}} \exp\left(-\frac{t_{\text{H}_2\text{O}}}{\lambda_{\text{H}_2\text{O}}}\right) \left[\theta_{\text{OH}} \exp\left(-\frac{t_{\text{OH}}}{\lambda_{\text{OH}}}\right) + \theta_{\text{CO}_3} \exp\left(-\frac{t_{\text{CO}_3}}{\lambda_{\text{CO}_3}}\right) + (1 - \theta_{\text{OH}} - \theta_{\text{CO}_3}) \right] \left[1 - \exp\left(-\frac{t_{\text{surf}}}{\lambda_{\text{surf}}}\right) \right] \quad (1d)$$

$$I_{\text{ox}} \sim N_{\text{ox}} \sigma_{\text{ox}} \lambda_{\text{ox}} \exp\left(-\frac{t_{\text{H}_2\text{O}}}{\lambda_{\text{H}_2\text{O}}}\right) \left[\theta_{\text{OH}} \exp\left(-\frac{t_{\text{OH}}}{\lambda_{\text{OH}}}\right) + \theta_{\text{CO}_3} \exp\left(-\frac{t_{\text{CO}_3}}{\lambda_{\text{CO}_3}}\right) + (1 - \theta_{\text{OH}} - \theta_{\text{CO}_3}) \right] \exp\left(-\frac{t_{\text{surf}}}{\lambda_{\text{surf}}}\right) \quad (1e)$$

By taking the intensity ratios, the variables t_{surf} , θ_{OH} , θ_{CO_3} and $t_{\text{H}_2\text{O}}$ are uniquely determined:

$$t_{\text{surf}} = \lambda_{\text{surf}} \ln(1 + R_{\text{ox}}^{\text{surf}}) \quad (2)$$

$$\text{where } R_j^i \equiv \frac{I_i}{I_j} \left(\frac{N_j \sigma_j \lambda_j}{N_i \sigma_i \lambda_i} \right)$$

$$\begin{bmatrix} \frac{\exp\left(\frac{t_{\text{surf}}}{\lambda_{\text{surf}}}\right)}{R_{\text{ox}}^{\text{OH}}} + a_{\text{OH}}^* - a_{\text{OH}}^{\text{OH}} & a_{\text{OH}}^* - a_{\text{OH}}^{\text{CO}_3} \\ a_{\text{CO}_3}^* - a_{\text{CO}_3}^{\text{OH}} & \frac{\exp\left(\frac{t_{\text{surf}}}{\lambda_{\text{surf}}}\right)}{R_{\text{ox}}^{\text{CO}_3}} + a_{\text{CO}_3}^* - a_{\text{CO}_3}^{\text{CO}_3} \end{bmatrix} \begin{bmatrix} \theta_{\text{OH}} \\ \theta_{\text{CO}_3} \end{bmatrix} = \begin{bmatrix} a_{\text{OH}}^* \\ a_{\text{CO}_3}^* \end{bmatrix} \quad (3)$$

$$\text{where } a_j^* \equiv \frac{1}{1 - \exp\left(-\frac{t_j}{\lambda_j}\right)} ; \quad a_j^i \equiv a_j^* \exp\left(-\frac{t_i}{\lambda_i}\right)$$

$$t_{\text{H}_2\text{O}} = \lambda_{\text{H}_2\text{O}} \ln\left(\frac{1 + b_{\text{H}_2\text{O}}}{b_{\text{H}_2\text{O}}}\right) \quad (4)$$

$$\text{where } b_{\text{H}_2\text{O}} \equiv \left\{ R_{\text{ox}}^{\text{H}_2\text{O}} \left[\theta_{\text{OH}} \exp\left(-\frac{t_{\text{OH}}}{\lambda_{\text{OH}}}\right) + \theta_{\text{CO}_3} \exp\left(-\frac{t_{\text{CO}_3}}{\lambda_{\text{CO}_3}}\right) + (1 - \theta_{\text{OH}} - \theta_{\text{CO}_3}) \right] \exp\left(-\frac{t_{\text{surf}}}{\lambda_{\text{surf}}}\right) \right\}^{-1}$$

Finally, the thickness of the water layer ($t_{\text{H}_2\text{O}}$) was used to estimate the water surface coverage

$\theta_{\text{H}_2\text{O}}$ by normalizing to the size of the water molecule ($\theta_{\text{H}_2\text{O}} = \frac{t_{\text{H}_2\text{O}}}{3.1 \text{ \AA}})^3$. It is noted that the fitted

thickness of the surface oxygen layer is on the order of a few atomic layers (**Fig. S9**, Supporting Information), which is consistent with the length-scale of a reconstructed surface, and it did not change significantly as a function of RH. **Table S4** provides the constants used in the electron attenuation model.

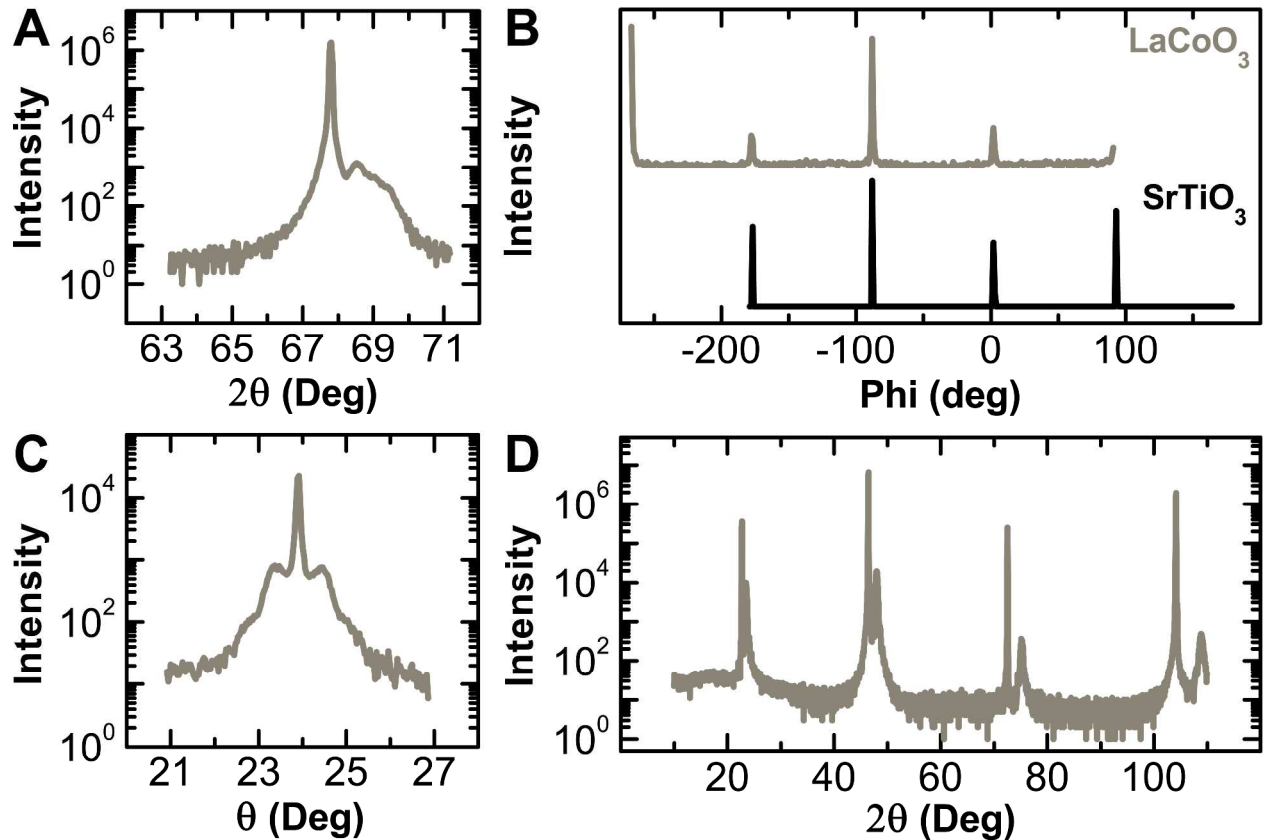


Figure S1. (A) Off-normal 2θ - ω scan of the $(202)_{pc}$ reflections. (B) Φ scan in-plane, aligned to the $(202)_{pc}$ reflections of the LaCoO_3 (gray, top) and the Nb-doped SrTiO_3 (black, bottom) substrate. (C) Rocking curve at the $(001)_{pc}$ reflection. Satellite peaks in LCO films have been reported to originate from both periodic twinning modulation and lattice plane tilt.⁴ (D) Long range 2θ - ω scan in the normal orientation.

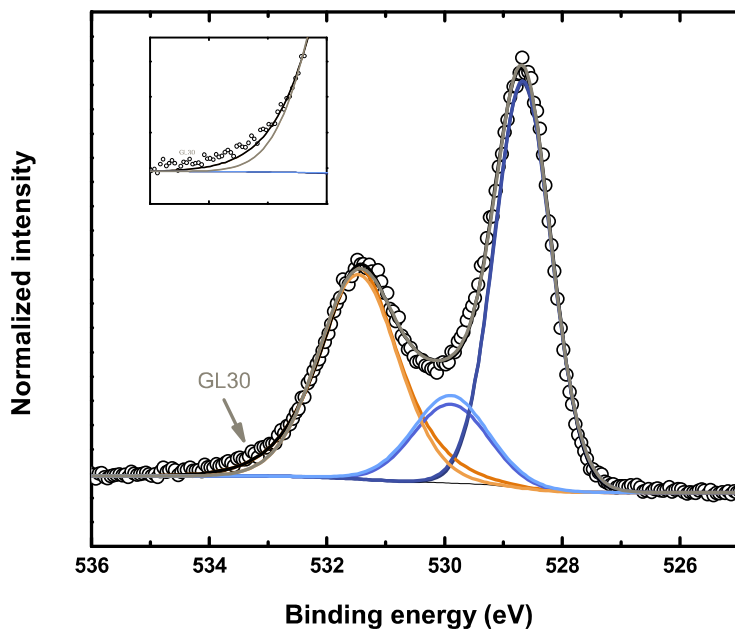


Figure S2: Fit in the main text of O 1s at 735 eV in 100 mTorr O₂ at 300°C (dark components, black envelope) and fit using a constant GL ratio of 30 (lighter components; gray envelope). The high binding energy tail is only fit using a higher Lorentzian ratio, shown with a zoom-in of intensity in the inset.

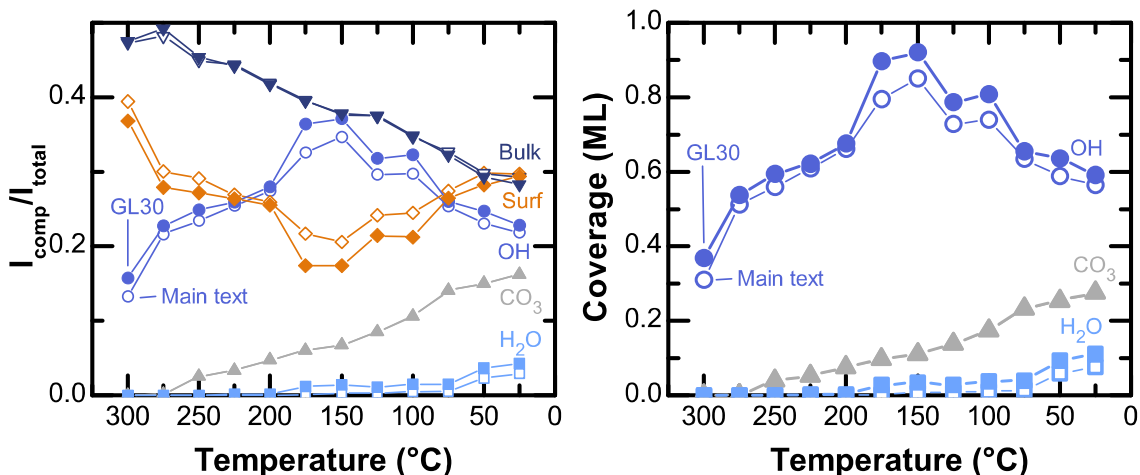


Figure S3: Intensity of each component relative to the total O 1s intensity (left) and coverage (right) for fits in the main text (open) compared to that when a constant Gaussian-Lorentzian (GL) ratio of 30 was used (solid). A constant GL ratio slightly increases the OH and adsorbed water intensity (open corresponds to a GL ratio of 0) at the expense of the surface peak (open GL ratio of 70). The difference in coverage calculated with the two different fitting routines is effectively an error based on differences in peak shape; deviations between the GL30 and Main Text data points are illustrative of the level of error associated with peak fitting constraints.

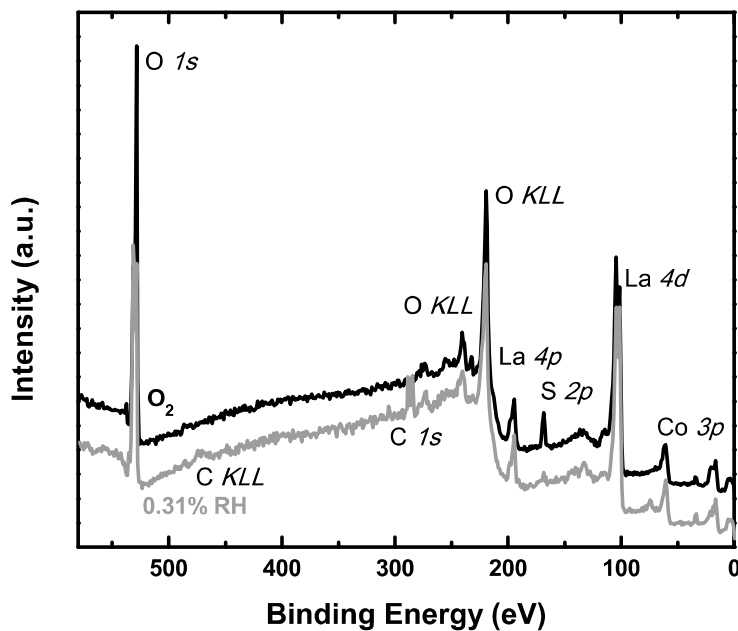


Figure S4. Survey spectra at 735 eV incident energy, at 300 °C in O₂ (black, top) and 25 °C in H₂O (gray, bottom). Only expected elements (La, Co, O) are observed when cleaning in O₂, except for sulfur, which is known to bind strongly to perovskites in such conditions.⁵ No sulfur was observed in films prior to cleaning, and the amount decreased upon changing the environment from O₂ to H₂O, as well as reducing the temperature. The potential contribution of sulfate to the O 1s is discussed in **Fig. S5**. At 25 °C in water, carbon is present, but sulfur is negligible. A small peak at 75 eV appeared after the isobar experiments at 25 °C in water, which is consistent with the Al 2p core level. However, no features in the O 1s spectra were consistent with the hydroxylation (534.6 eV) and wetting (536.6 eV) of Al₂O₃.⁶

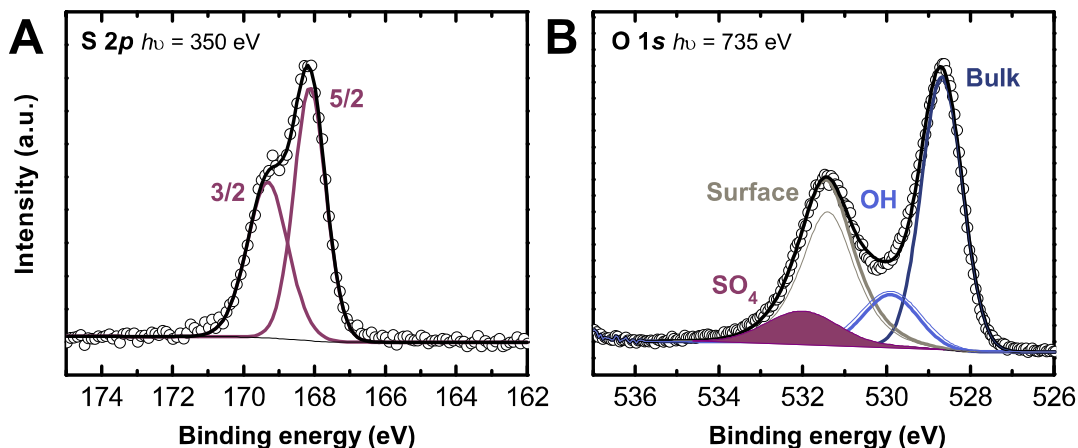


Figure S5. Sulfur was observed when the LCO was heated to 300 °C in O₂. (A) S 2*p* core level at an incident photon energy of 350 eV, with binding energy typical of that for lanthanum and transition metal sulfates.⁵ The sulfate O 1*s* binding energy is 532-533 eV.⁵ (B) In order to estimate the maximum potential contribution of sulfate to the O 1*s*, the S 2*p* intensity was scaled by the ratio of the tabulated cross sections of C 1*s* at 735 eV to S 2*p* at 350 eV ($\sigma_S = 0.1339 \sigma_{C1s}$)^{7,8} the measured RSF of O 1*s* to C 1*s* at 735 eV (RSF = 0.83), and the oxygen stoichiometry of sulfate (O:S = 4:1). Including possible sulfate contribution (purple) reduces the quantity of the surface oxygen species (thin gray line), but only by ~20%.

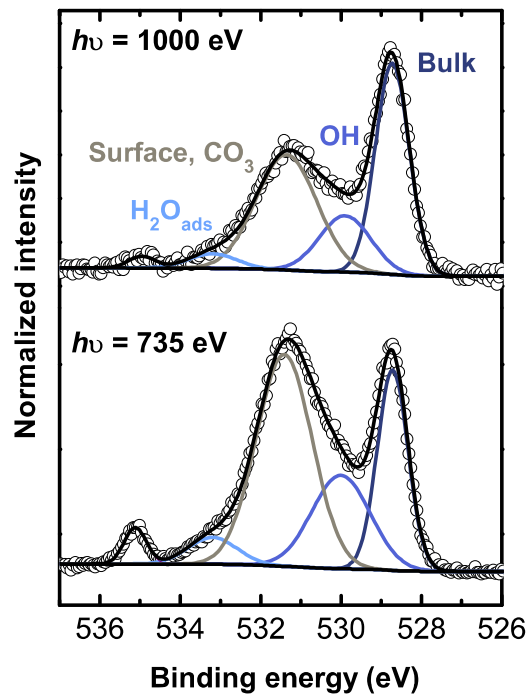


Figure S6. O 1s spectra at 1000 eV and 735 eV incident photon energy and fixed beam spot. Spectra were collected for a film at 25°C in 100 mTorr H₂O and are shown normalized to the maximum intensity. The shallower information depth at 735 eV incident photon energy enhances the contribution from the OH (medium blue), H₂O_{ads} (light blue), and “Surface” oxygen/CO₃ (gray) and lessens that of the “Bulk” oxidic peak (dark blue). Unlike other O 1s spectra presented, these were collected at a fixed spot without closing the shutter in between measurements, and have a higher CO₃ contribution. The CO₃ and “Surface” oxygen are not deconvoluted separately for this case as the RSF of O:C at 1000 eV incident photon energy was not measured.

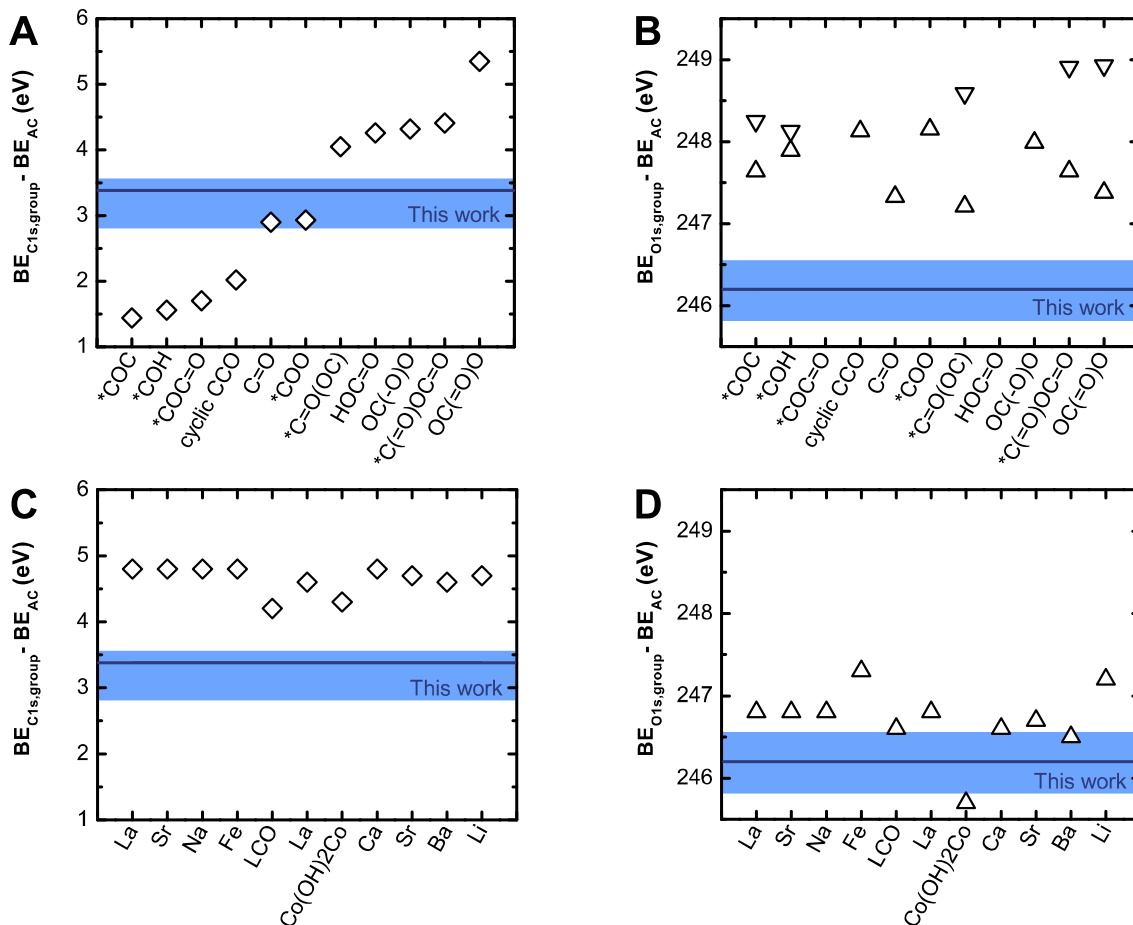


Figure S7. Comparison of relative binding energy (BE) shifts for different previously reported functional groups to that measured in this work for the assigned CO₃ species. The value for “This work” is an average for the LCO-nonrotating isobar, with the shaded box covering the minimum and maximum measured value. (A) C 1s and (B) O 1s BE of carbon functional groups relative to adventitious hydrocarbon.^{9, 10} (C) C 1s and (D) O 1s BE of previously reported transition metal,¹¹⁻¹³ lanthanide,^{11, 13} group II,¹⁴ and lithium¹⁵ carbonates.

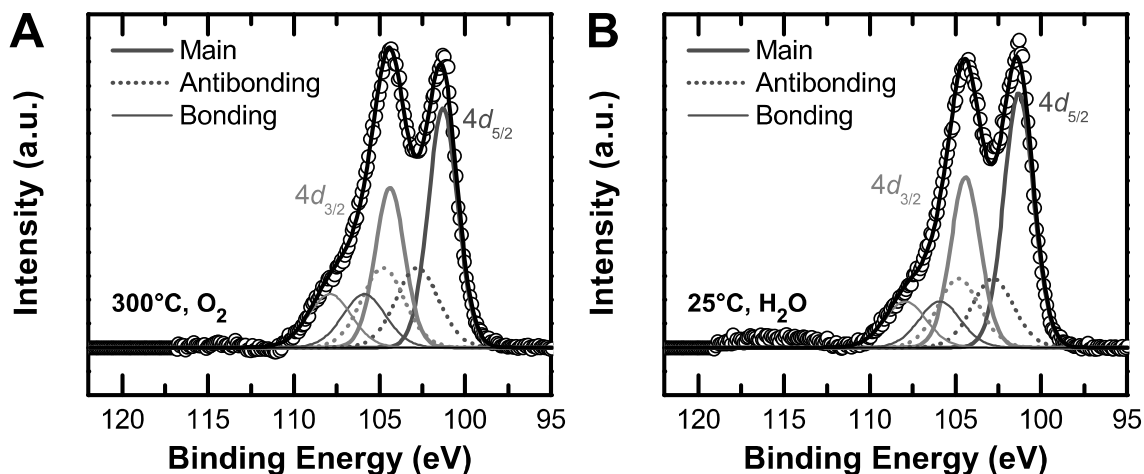


Figure S8. La $4d$ spectra at 735 eV incident photon energy taken at the same beam location for (A) a clean film at 300 °C in 100 mTorr O_2 and (B) a film at 25 °C in 100 mTorr H_2O . The spectra are composed of spin-orbit split $4d_{5/2}$ and $4d_{3/2}$ contributions (3.1 eV split), and satellite features associated with bonding (3.5 eV from main peak) and antibonding (1.5 eV from main peak) charge-transferred states are present in addition to the main peak. In addition to constraining the relative peak positions for the three components, the relative areas and FWHM of the $4d_{3/2}$ spin-orbit split peaks (high binding energy set) were also fixed, allowing for four free fitting parameters: binding energy of the main peak, and integrated areas for the $4d_{5/2}$ (low binding energy set) main, antibonding, and bonding peaks.

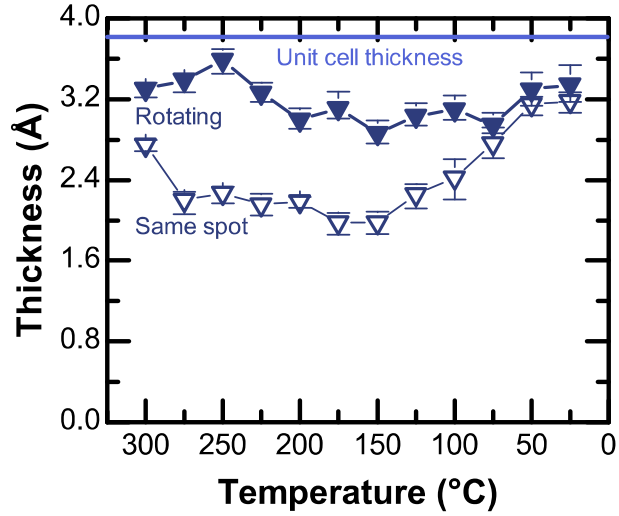


Figure S9. Thickness of the “Surface” oxygen layer obtained from the multilayer electron attenuation model. We note the calculated thickness is on the order of one or two atomic layers, close to that of a full unit cell of the LCO perovskite ($t_{\text{LCO}} = 3.8 \text{ \AA}$). The slightly thicker layer for the rotating analysis spot (filled) compared to when the same spot was irradiated (open) corresponds to a thinner overlayer of adsorbates in the former case, compared in **Fig. 10** of the main text. Error bars are defined as the 95% confidence intervals estimated from Monte Carlo simulations.

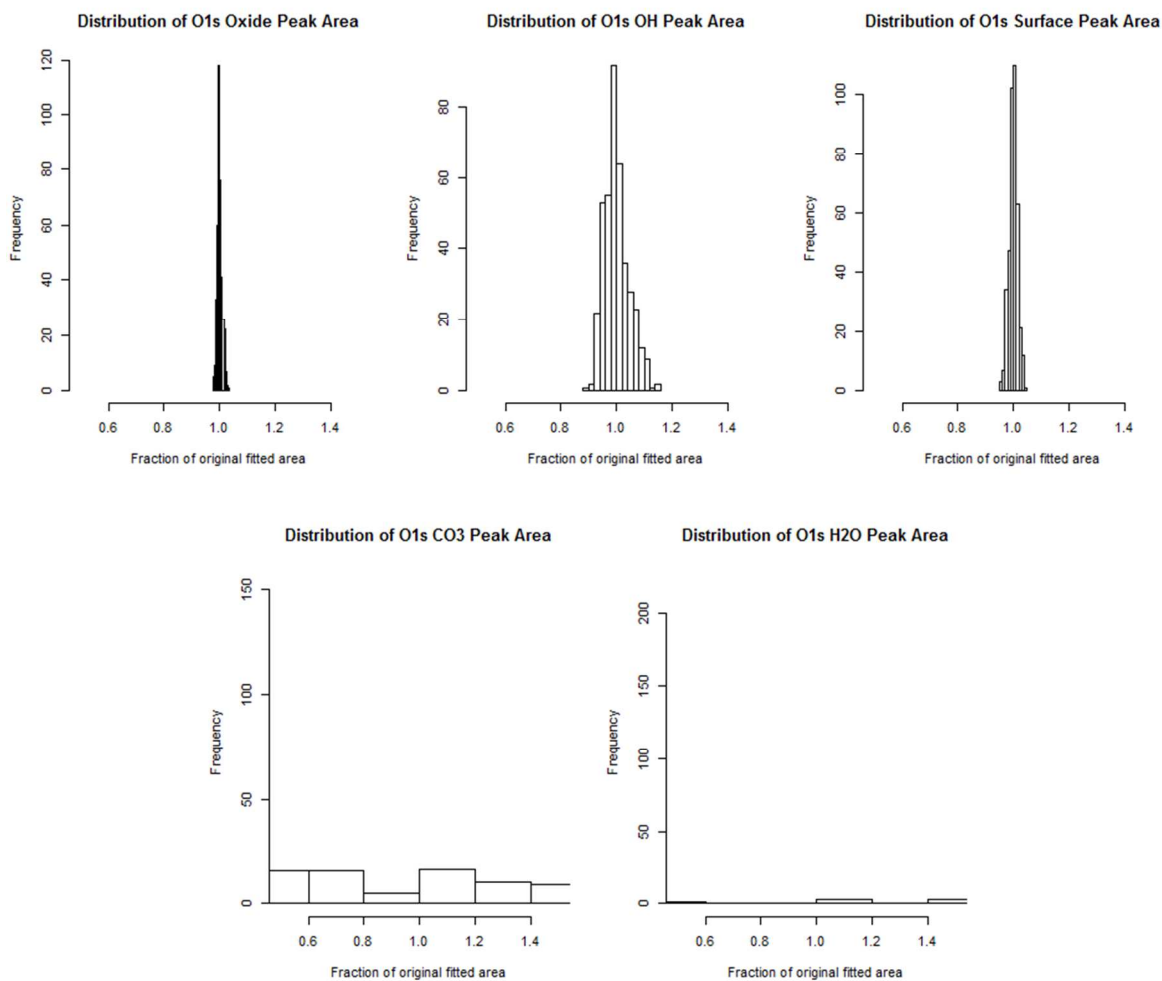


Figure S10. Histograms of the fitted O 1s peak areas at 300 °C and 0.1 Torr H₂O for 400 Monte Carlo simulations implementing artificial experimental noise (shown with equal number of bins for each species). Note the wider spread and non-normal distributions that can result from the correlation between peak components with low intensities (e.g., OH, CO₃, and H₂O_{ads}). The low areas for CO₃ and H₂O_{ads} species results in a distribution wider than the range of the x-axis.

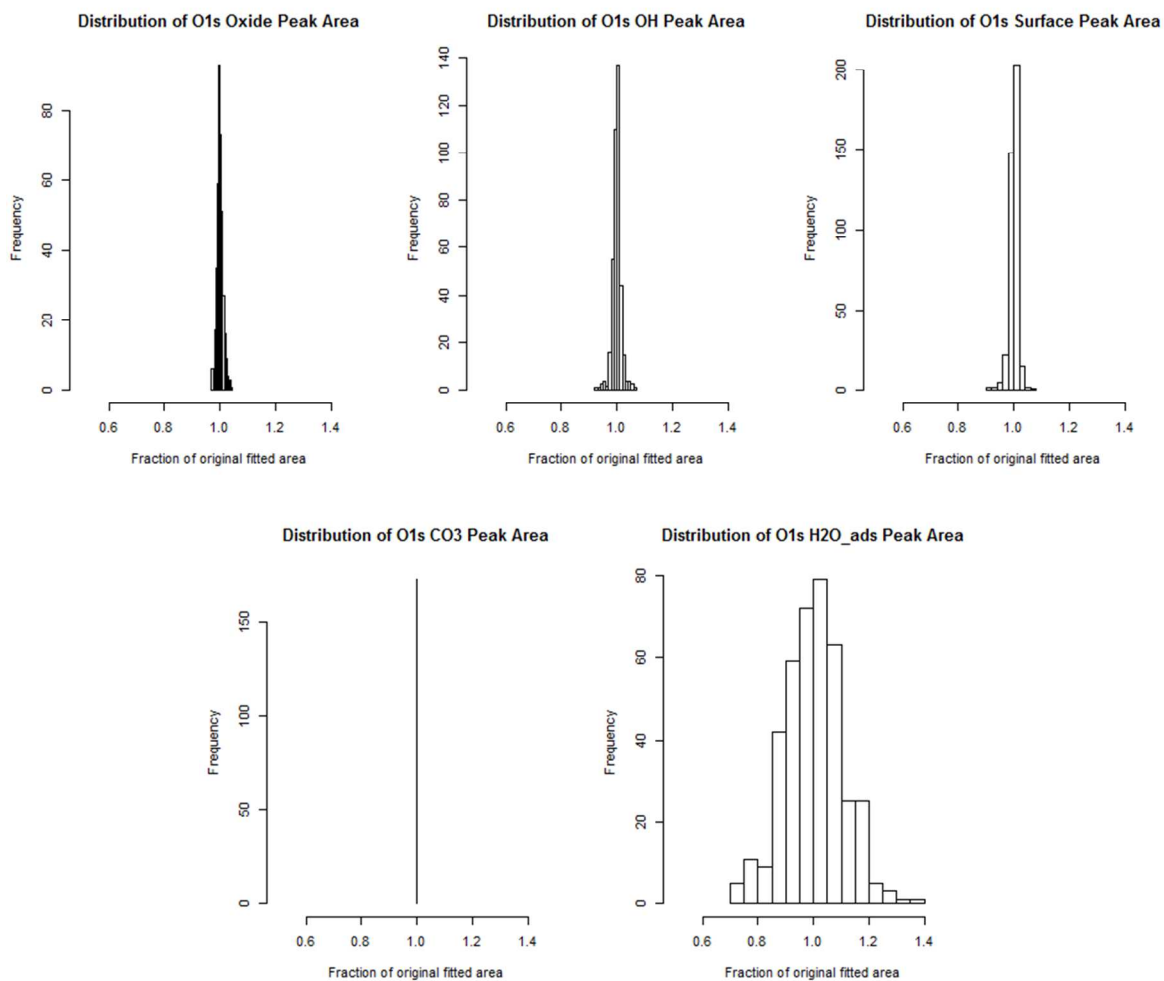


Figure S11. Histograms of the fitted O 1s peak areas at 50 °C and 0.1 Torr H₂O for 400 Monte Carlo simulations implementing artificial experimental noise (shown with equal number of bins for each species). With the better defined peak features in the raw spectra, the spreads are significantly reduced and the fitted peak areas approach normal-like distributions.

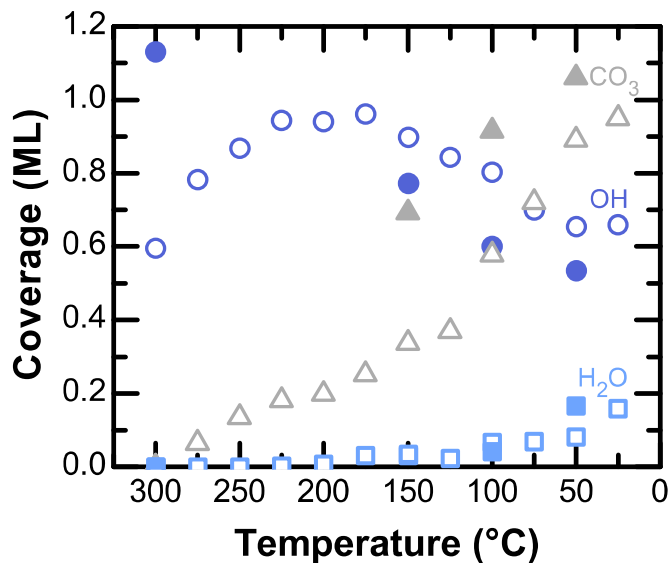


Figure S12. Coverage of surface species on LCO as a function of temperature in 100 mTorr H₂O: adsorbed H₂O (\square , light blue), CO₃ (Δ , gray), and OH (O, medium blue). This measurement – performed at ALS 11.0.2 under two-bunch operation – can be compared with Fig. 9 of the main text, measured under multi-bunch operation during a different beamtime. Open circles indicate coverage from measurements performed as a function of decreasing temperature, and filled circles indicate measurements testing for reversibility by increasing the temperature from 25 °C to 300 °C. Similar trends in the evolution of surface species were observed: an initial growth of OH, CO₃ formation at the expense of OH coverage, and H₂O adsorption at high relative humidity/low temperature, with greater θ_{CO_3} in Fig. S12 resulting from higher residual carbon in the XPS chamber from previous measurements. In the subsequent heating, H₂O adsorption/desorption appeared to be largely reversible. Similarly, the trend in θ_{CO_3} qualitatively suggests that its adsorption/desorption is reversible, but this cannot be quantitatively evaluated because measurements were performed out of equilibrium with the intent of minimizing CO₃ coverage. In contrast, OH adsorption/desorption was not reversible, and θ_{OH} was found to increase upon heating. The coverage was much greater returning to 300 °C than that initially obtained introducing H₂O into the chamber with the O₂-cleaned surface at 300 °C, which is in agreement with strongly-bound OH sites observed even in oxidative environments.

Table S1. Peak fitting parameters for the O 1s spectra of LCO films. Peak assignments were made assuming the minimum number of peaks necessary to fit spectral features. Binding energies (BE – maxima and minima reported) and full-width-half-maxima (FWHM) agree well with values reported in literature.¹⁶⁻¹⁸

	Bulk	Surface	OH	CO₃	H₂O_{ads}	H₂O_{gas}
% Lorentzian	10	70	0	0	0	0
LaCoO₃ FWHM (eV)	0.9-1.2	1.5-1.7	1.5-1.7	1.5-1.7	1.4-1.5	0.5-1.0
BE_{low}-BE_{high} (eV)	528.6-528.8	531.4-531.7	529.9-530.2	531.2-531.7	533.2-533.3	533.9-535

Table S2. Raw intensity of fitted O 1s using fitting parameters from the main text, for the sample analyzed at fixed beam spot.

Gas	T [°C]	I_{ox} [cps]	I_{surface} [cps]	I_{OH} [cps]	I_{CO₃} [cps]	I_{H₂O_{ads}} [cps]	I_{H₂O_{gas}} [cps]
O ₂	300	30954.9	27502.8	7597.2			
H ₂ O	300	32715.5	27263.1	9163.8	1	0	807.9
	275	32056.8	20024.4	14415.5	84	0	642
	250	29503.2	19146.4	15413.4	1664	0.2	791.7
	225	28950.4	17606	16587.6	2165	0	784.9
	200	27221.9	16853.5	17808.9	3082.2	0.6	784.5
	175	25637.4	14041.3	21075.5	3903	73.9	851.7
	150	23996.5	13102.1	22065.2	4317	221.5	1015.9
	125	23485.6	15143	18609	5334.9	190.8	1021.2
	100	21341.6	15060.3	18317.5	6544	291	1067
	75	20029	16795.1	15524.1	8628	329.4	1148.8
	50	17636.8	17660.3	13622.6	8903.4	1356	1462.5
	25	16694.9	16964.9	12463.8	9226.9	1687.2	1130.8

Table S3. Percent intensity of fitted O 1s, relative to total O 1s LCO and surface species (excluding gas phase) using fitting parameters from the main text, for the sample analyzed at fixed beam spot.

Gas T		I _{ox} [%]	I _{surface} [%]	I _{OH} [%]	I _{CO₃} [%]	I _{H₂O_{ads}} [%]
	[°C]					
O ₂	300	46.86	41.64	11.50	0.00	0.00
H ₂ O	300	47.31	39.43	13.25	0.00	0.00
	275	48.15	30.07	21.65	0.13	0.00
	250	44.89	29.13	23.45	2.53	0.00
	225	44.33	26.96	25.40	3.31	0.00
	200	41.90	25.94	27.41	4.74	0.00
	175	39.61	21.69	32.56	6.03	0.11
	150	37.67	20.57	34.64	6.78	0.35
	125	37.42	24.13	29.65	8.50	0.30
	100	34.67	24.47	29.76	10.63	0.47
	75	32.67	27.40	25.32	14.07	0.54
	50	29.80	29.84	23.02	15.04	2.29
	25	29.27	29.74	21.85	16.18	2.96

Table S4. Constants used in the multilayer electron attenuation model. The inelastic mean free paths were calculated using the Gries inelastic scattering model and predictive equation with the density of reference compounds.¹⁹ Inelastic mean free paths and oxygen atomic densities for the OH and CO₃ layers were taken as the average of the transition metal and lanthanide reference compounds in order to account for the ambiguity of the surface termination.

Model layer	Thickness, t (Å)	Inelastic mean free path, λ (Å)	Oxygen atomic density, N (cm ⁻³ × 10 ²²)	Reference compounds
Bulk	n/a	4.53	5.36	LaCoO ₃ ²⁰
Surface	<i>calculated</i>	4.53	5.36	LaCoO ₃ ²⁰
OH	3.0	6.07	4.44	Co(OH) ₂ ¹ La(OH) ₃ ²¹
CO ₃	4.5	7.79	4.67	CoCO ₃ ¹ La ₂ (CO ₃) ₃ ¹
H ₂ O _{ads}	<i>calculated</i>	10.68	3.34	H ₂ O ³

References for Supporting Information

- (1) Perry, D. L., *Handbook of Inorganic Compounds*. 2 ed.; CRC Press: Boca Raton, FL, 2011.
- (2) Shinn, D. B.; Eick, H. A. The Crystal Structure of Lanthanum Carbonate Octahydrate. *Inorg. Chem.* **1968**, *7*, 1340-1342.
- (3) Tîmneanu, N.; Caleman, C.; Hajdu, J.; van der Spoel, D. Auger Electron Cascades in Water and Ice. *Chem. Phys.* **2004**, *299*, 277-283.
- (4) Fuchs, D.; Arac, E.; Pinta, C.; Schuppler, S.; Schneider, R.; v. Löhneysen, H. Tuning the Magnetic Properties of LaCoO₃ Thin Films by Epitaxial Strain. *Phys. Rev. B.* **2008**, *77*.
- (5) Liang, J.-J.; Weng, H.-S. XPS Analysis for the SO₂ Poisoning of Mn- and Co-series Perovskite Catalysts Used in Toluene Oxidation. *J. Environ. Eng. Manage.* **2007**, *17*.
- (6) Deng, X.; Herranz, T.; Weis, C.; Bluhm, H.; Salmeron, M. Adsorption of Water on Cu₂O and Al₂O₃ Thin Films. *J. Phys. Chem. C.* **2008**, *112*, 9668-9672.
- (7) Yeh, J. J., Atomic Calculation of Photoionization Cross-Sections and Asymmetry Parameters. Gordon and Breach Science Publishers: Langhorne, PE (USA), 1993.
- (8) Yeh, J. J.; Lindau, I. Atomic Data and Nuclear Data Tables. **1985**, *32*, 1-155.
- (9) Briggs, D.; Beamson, G. Primary and Secondary Oxygen-Induced C 1s Binding Energy Shifts in X-ray Photoelectron Spectroscopy of Polymers. *Anal. Chem.* **1992**, *64*, 1729-1736.
- (10) Briggs, D.; Beamson, G. XPS Studies of the Oxygen 1s and 2s Levels in a Wide Range of Functional Polymers. *Anal. Chem.* **1993**, *65*, 1517-1523.
- (11) Gonzalez-Elipe, A. R.; Espinos, J. P.; Fernandez, A.; Munuera, G. XPS Study of the Surface Carbonation/Hydroxylation State of Metal Oxides. *Appl. Surf. Sci.* **1990**, *45*, 103-108.
- (12) Heuer, J. K.; Stubbins, J. F. An XPS Characterization of FeCO₃ Films for CO₂ Corrosion. *Corros. Sci.* **1999**, *41*, 1231-1243.
- (13) Stoch, J.; Gablankowska-Kukucz, J. The Effect of Carbonate Contaminations on the XPS O 1s Band Structure in Metal Oxides. *Surf. Interface Anal.* **1991**, *17*, 165-167.
- (14) Christie, A. B.; Lee, J.; Sutherland, I.; Walls, J. M. An XPS Study of Ion-Induced Compositional Changes with Group II and Group IV Compounds. *Appl. Surf. Sci.* **1983**, *15*, 224-237.
- (15) Younesi, R.; Hahlin, M.; Roberts, M.; Edström, K. The SEI Layer Formed on Lithium Metal in the Presence of Oxygen: A Seldom Considered Component in the Development of the Li-O₂ Battery. *J. Power Sources.* **2013**, *225*, 40-45.
- (16) Ogletree, D. F.; Bluhm, H.; Lebedev, G.; Fadley, C. S.; Hussain, Z.; Salmeron, M. A Differentially Pumped Electrostatic Lens System for Photoemission Studies in the Millibar Range. *Rev. Sci. Instrum.* **2002**, *73*, 3872-3877.
- (17) Yamamoto, S.; Kendelewicz, T.; Newberg, J. T.; Ketteler, G.; Starr, D. E.; Mysak, E. R.; Andersson, K.; Ogasawara, H.; Bluhm, H.; Salmeron, M.; *et al.* Water Adsorption on α -Fe₂O₃(0001) at near Ambient Conditions. *J. Phys. Chem. C.* **2010**, *114*, 2256-2266.
- (18) Kendelewicz, T.; Kaya, S.; Newberg, J. T.; Bluhm, H.; Mulakaluri, N.; Moritz, W.; Scheffler, M.; Nilsson, A.; Pentcheva, R.; Brown, G. E. X-ray Photoemission and Density Functional Theory Study of the Interaction of Water Vapor with the Fe₃O₄(001) Surface at Near-Ambient Conditions. *J. Phys. Chem. C.* **2013**, *117*, 2719-2733.

- (19) Gries, W. H. A Universal Predictive Equation for the Inelastic Mean Free Pathlengths of X-ray Photoelectrons and Auger Electrons. *Surf. Interface Anal.* **1996**, *24*, 38-50.
- (20) Pathak, S.; Kuebler, J.; Payzant, A.; Orlovskaya, N. Mechanical Behavior and Electrical Conductivity of $\text{La}_{1-x}\text{Ca}_x\text{CoO}_3$ ($x=0, 0.2, 0.4, 0.55$) Perovskites. *J. Power Sources.* **2010**, *195*, 3612-3620.
- (21) Shannon, R. D. Dielectric Polarizabilities of Ions in Oxides and Fluorides. *J. Appl. Phys.* **1993**, *73*, 348-366.